Evaluation of Nanostructured β-Mn$_2$V$_2$O$_7$ Thin Films as Photoanodes for Photoelectrochemical Water Oxidation

Yash Gargasya, Melissa K. Gish, Vineet V. Nair, Justin C. Johnson, and Matt Law*

ACCESS | Metrics & More | Article Recommendations | SI Supporting Information

ABSTRACT: β-Mn$_2$V$_2$O$_7$ (β-MVO) was recently reported to be a promising candidate for photoelectrochemical (PEC) water splitting, with a suitable band gap and band edge positions and reasonable stability and photoactivity in preliminary tests in alkaline solution. Here, we present an in-depth evaluation of the PEC performance and stability of phase-pure nanostructured β-Mn$_2$V$_2$O$_7$ films made by calcination of a spin-cast molecular ink. We show that β-Mn$_2$V$_2$O$_7$ dissolves in pure water, corrodes in aqueous electrolytes at pH 7 and 9, and converts to amorphous manganese (hydr)oxides within minutes at pH 13. Our β-Mn$_2$V$_2$O$_7$ films yielded only miniscule photocurrents ($\sim \mu$A cm^{-2}) for the oxidation of iodide, sulfite, or water and the reduction of iodate or water in borate- and phosphate-buffered electrolytes at pH 7 and 9, the oxidation of $[Fe(CN)_6]^{4-}$ or water at pH 13, and the oxidation of bromide in acetonitrile, regardless of film calcination temperature and time, film thickness, and illumination geometry. Minimal photoactivity was observed even in electrolytes in which film degradation was insignificant over the duration of the PEC tests. Ultrafast transient absorption spectroscopy shows that the poor photoactivity is likely the result of fast hole trapping and recombination at the MVO surface that leaves few free charge carriers beyond the picosecond time scale. Given its poor charge transport/extraction and chemical stability, native nanostructured β-Mn$_2$V$_2$O$_7$ is ineffective for solar water splitting and future research on this material should focus on the development of superior syntheses and film morphologies, MVO alloys, heterostructures, and surface coatings to alleviate recombination and boost operational stability. This work underscores the importance of careful follow-up studies of materials identified as "hits" in combinatorial materials discovery campaigns.
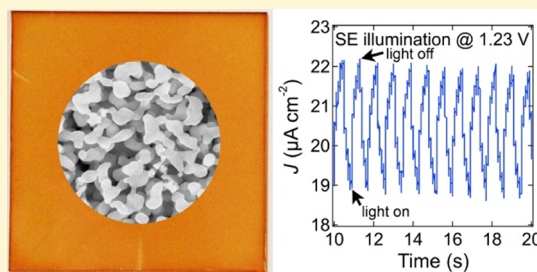
1. INTRODUCTION

The discovery of efficient, stable, and inexpensive photoanode materials for use in tandem photoelectrochemical (PEC) water splitting devices remains a major challenge to the realization of practical solar-driven hydrogen production.[1−3] In 2015, Yan et al. reported β-Mn$_2$V$_2$O$_7$ (β-MVO) as a highly promising n-type semiconductor for solar water splitting, with a near-optimal optical band gap energy of 1.75 ± 0.1 eV,[4] band edge energies that straddle the water oxidation and reduction potentials, and electrochemical stability under illumination in the pH 13 electrolyte.[5] These authors prepared bulk powders by chloride salt calcination. X-ray diffraction (XRD) showed that the powders consisted of a mixture of β-Mn$_2$V$_2$O$_7$, α-Mn$_2$V$_2$O$_7$, and at least one unidentified crystalline phase. Diffuse reflectance spectra of these mixed-phase samples were used to estimate the optical band gap of β-Mn$_2$V$_2$O$_7$. Films with a composition of "Mn$_{0.5}$V$_{0.5}$O$_x$" were then made by a similar but different procedure and evaluated for their photoactivity in the pH 13 electrolyte. However, no characterization of the phase composition or optical properties of the films before or after PEC testing was presented. An anodic photocurrent of $\sim$0.1 mA cm^{-2} was reported for the Mn$_{0.5}$V$_{0.5}$O$_x$ films in 0.1 M NaOH (aq) with $[Fe(CN)_6]^{3-/4-}$ (a fast redox couple) when biased at $\sim$1.1 V versus the reversible hydrogen electrode

(RHE) and illuminated with chopped ultraviolet light (3.2 eV), but no photocurrent was observed in the absence of the $[Fe(CN)_6]^{4-}$ hole scavenger, indicating that the samples were not appreciably photoactive for the oxygen evolution reaction (OER). The report by Yan et al. generated significant interest in β-Mn$_2$V$_2$O$_7$ as a candidate water splitting material,[1−3,6−9] but it also raised many questions, including whether their films were in fact β-Mn$_2$V$_2$O$_7$ and stable in base.

There has been little subsequent experimental work on MVO in the context of water splitting. Abdi and Berglund mentioned parenthetically that transient microwave conductivity measurements revealed β-Mn$_2$V$_2$O$_7$ to have a low mobility of $\sim$10^{-4} cm^2 V^{-1} s^{-1}, suggesting that the small photocurrent reported by Yan et al. is caused by a short carrier diffusion length in this material.[2] Very recently, Seenivasan and co-workers reported a surprisingly long minority carrier
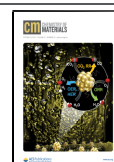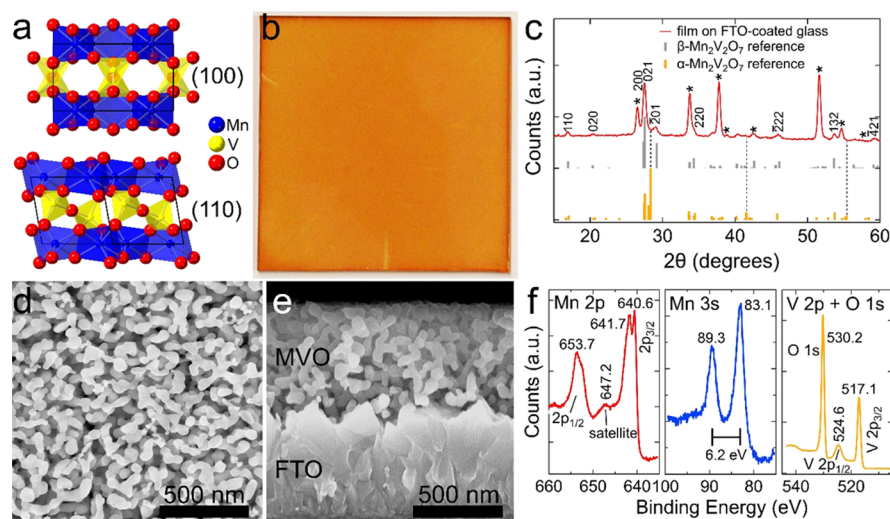
Figure 1. Characterization of nanostructured MVO thin films on FTO-coated glass substrates. (a) Polyhedral representations of the monoclinic β-$Mn_2V_2O_7$ crystal structure. (100) and (110) projections highlight the layered structure and isolated $V_2O_7^{4-}$ units (yellow). The unit cell is outlined with black lines. (b) Photograph of a 580 ± 60 nm-thick β-MVO film deposited on a 3×3 inch FTO-coated glass substrate by spin-coating and calcining the molecular ink. (c) XRD pattern of a duplicate film. All peaks index to β-$Mn_2V_2O_7$ (PDF# 01-089-0484, gray bars), although the presence of a trace amount of α-$Mn_2V_2O_7$ (PDF# 01-089-0483, orange bars) cannot be ruled out in these data (dotted lines). FTO substrate peaks are denoted with asterisks. (d,e) Plan-view and cross-sectional scanning electron microscopy (SEM) images of the film. (f) XPS spectra of the Mn 2p, Mn 3s, and V 2p regions with binding energies labeled. See Figure S1 for synchrotron XRD data, Figure S2 for corresponding data for films on quartz substrates, Figure S3 for Raman spectra of films on both substrates, and Figure S4 for characterization of nonporous MVO films made from inks without the triblock copolymer.

diffusion length of ~235 nm and photocurrents of up to ~0.15 mA cm^{-2} from mixed-phase β-$Mn_2V_2O_7$ films that contained molybdenum and were encapsulated in a TiO_2 coating by atomic layer deposition and measured under simulated sunlight in borate buffer at pH 9.[9] $Mn_2V_2O_7$ has two well-known polymorphs, a low-temperature triclinic phase (α-$Mn_2V_2O_7$) and the high-temperature monoclinic phase (β-$Mn_2V_2O_7$), which reversibly interconvert via a thermally hysteretic first-order phase transition over a temperature range of 285–310 K.[10−12] Most experimental studies of $Mn_2V_2O_7$ have focused either on its $\beta−\alpha$ phase transition and low-temperature magnetic ordering[10−15] or applications in lithium-ion batteries,[16−18] solar cells,[19] and (electro)-catalysis.[20−22]

Many detailed investigations of other candidate water splitting materials have been reported using a variety of methodologies and characterization techniques. For example, Toma *et al.* used X-ray photoelectron spectroscopy (XPS), Rutherford backscattering spectrometry, inductively coupled plasma mass spectrometry (ICP-MS), electron microscopy, and *in situ* electrochemical atomic force microscopy to study the mechanism of chemical and PEC transformation of $BiVO_4$.[23] Zhou *et al.* used combinatorial scanning electrochemical probes and XPS, along with XRD, X-ray fluorescence, and energy-dispersive spectroscopy to study the chemical instability of copper vanadate.[24] Pourbaix diagrams were used to explain the experimental results in both of these studies. Knöppel et al. used a PEC scanning flow cell coupled with real-time ICP-MS to study the effect of electrolyte counterions on the photocorrosion of WO_3.[25]

Here, we evaluate the stability and PEC performance of phase-pure films of nanostructured β-$Mn_2V_2O_7$ made by calcination of a spin-cast molecular ink. We show that β-$Mn_2V_2O_7$ is unstable in pure water at pH 5.8 and aqueous electrolytes at pH 7 and 9. At pH 13, it corrodes within

minutes to form amorphous $Mn_xO_y(OH)_z$ phases. Our β-$Mn_2V_2O_7$ films yielded only miniscule photocurrents (~μA cm^{-2}) for the oxidation of iodide, sulfite, or water and the reduction of iodate or water in borate- and phosphate-buffered electrolytes at pH 7 and 9, the oxidation of $[Fe(CN)_6]^{4-}$ or water at pH 13, and the oxidation of bromide in acetonitrile, regardless of calcination temperature and time (which tune the crystallite size), film thickness, and illumination geometry. Minimal photoactivity was observed even in electrolytes in which film degradation was insignificant over the duration of the PEC tests. Ultrafast transient absorption spectroscopy (TAS) suggests that the poor photoactivity is mainly the result of fast hole trapping and recombination at the MVO surface that leaves few free charge carriers beyond the ps time scale. Given its poor charge transport and stability—particularly in alkaline solution—pure, nanostructured β-$Mn_2V_2O_7$ is not a promising photoanode material for solar water splitting, but exploration of other MVO preparation methods and film morphologies and systematic studies of doping/alloying, heterostructuring, and surface protection and catalyst coatings may still prove to be fruitful.

2. RESULTS AND DISCUSSION

2.1. Film Fabrication and Characterization. Monoclinic $Mn_2V_2O_7$ (β-MVO, Figure 1a) thin films were fabricated by spin-coating an acidified water-ethylene glycol ink of manganese(II) acetate tetrahydrate ($Mn(CH_3COO)_2 \cdot 4H_2O$), vanadium(IV) oxide acetylacetonate ($VO(acac)_2$), and a polyethylene−polypropylene−polyethylene triblock copolymer (Pluronic F-108) onto a substrate and calcining the dried ink layer in air (see the Experimental Section). The acid in the ink prevents the precipitation of vanadium, while the triblock copolymer is a thickening and structure-directing agent that produces porous nanocrystalline MVO films of tunable thickness, as we reported in the synthesis of similar $BiVO_4$
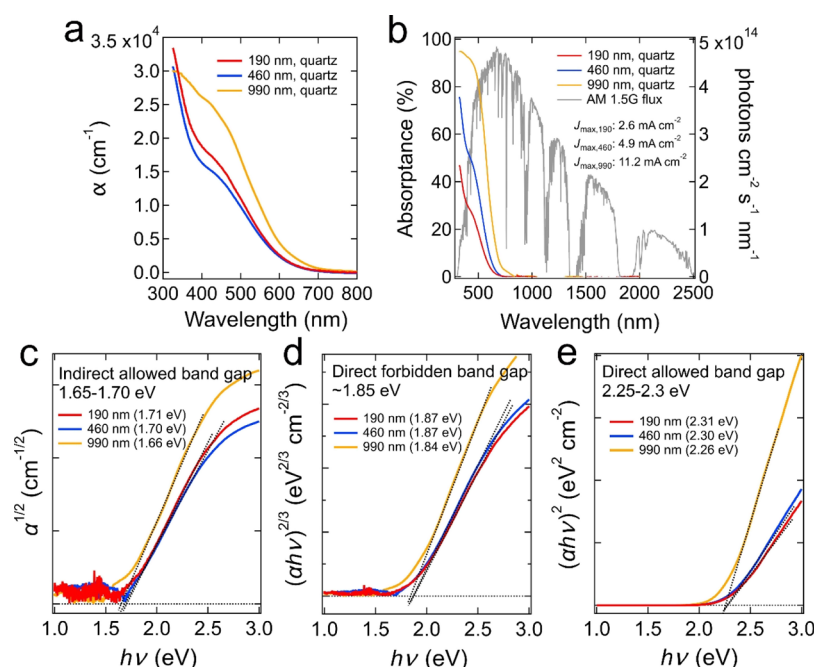
Figure 2. Absorptivity spectra and Tauc-style plots for MVO films on quartz substrates. (a) Absorptivity spectra for 190, 460, and 990 nm-thick MVO films. (b) Overlap of the absorptance spectra with the AM1.5G solar photon flux used to determine the maximum theoretical photocurrent for these films. Tauc plots and fits for an (c) indirect allowed transition, (d) direct forbidden transition, and (e) direct allowed transition. The estimated band gap of each sample is listed in the legends.

(BVO) films.[26] Figure 1 presents structural characterization data of our standard ~580 nm-thick MVO films made on fluorine-doped tin oxide (FTO)-coated glass substrates using a 30 min calcination at 500 °C. The films are bright orange, uniform across many square inches, optically smooth, and highly transparent (Figure 1b). XRD patterns of the films are consistent with phase-pure, untextured β-MVO (Figure 1c), but the presence of a trace α-MVO impurity cannot be ruled out from these data alone. High-resolution synchrotron powder XRD of powderized films showed phase-pure β-MVO and no evidence for α-MVO or other phase impurities (Figure S1). Films grown on quartz substrates also appeared to be pure, untextured β-MVO by XRD (Figure S2). Given the unknown effect of α-MVO impurities on the PEC behavior of β-MVO films, we restricted our study to these pure β-MVO films, leaving the investigation of α–β mixtures and pure α-MVO films for future work.

The β-MVO films have a comparable morphology and thickness on FTO-coated glass and quartz substrates. SEM images show that the standard films consist of a highly porous, sponge-like network of fused nanocrystals with a crystallite diameter of 53 ± 11 nm and a total film thickness of ~575 nm (Figures 1d,e and S2). This morphology offers a reasonable balance of small crystallite size, large film surface area, and good intercrystallite connectivity, which together are expected to favor the efficient transport of photogenerated holes to the MVO/water interface and electrons into the substrate. BVO films with a nearly identical microstructure made by a similar process were highly photoactive for both sulfite and water oxidation.[26]

We used XPS to determine the surface composition of the as-made MVO films on FTO-coated glass substrates. Manganese, vanadium, oxygen, carbon, potassium, and tin (from the substrate) were the only elements detected in XPS survey scans (Figure S5). High-resolution Mn 2p, Mn 3s, and

V 2p spectra are consistent with Mn^{2+} and V^{5+}, with no evidence for other oxidation states (Figures 1f and S5).[27−29] A Mn/V/O atomic ratio of 1.09:1:4.86 was determined from the XPS data. This value agrees well with a bulk Mn/V ratio of 1.02 ± 0.05 determined by ICP-MS of digested films and suggests that the as-made films are stoichiometric or nearly-stoichiometric $Mn_2V_2O_7$, possibly with a small excess of surface Mn.

We found that the thickness and average crystallite size of the β-MVO films could be independently tuned by adjusting the ink composition and film fabrication conditions. The film thickness was tuned from 150 nm to 4.6 μm—while maintaining phase purity, average crystallite size, and film morphology—by changing the solvent volume and spin speed while keeping the ink stoichiometry, annealing temperature, and annealing time constant (Table S1). XRD shows that all of the films were pure β-MVO, and SEM indicates an average crystallite diameter of 55−65 nm (Figure S6). The average crystallite diameter was tuned from 25 to 160 nm by changing the calcination temperature or time. For example, films calcined at 500 °C for 15, 60, or 120 min yielded a crystallite diameter of 39 ± 13, 89 ± 21, and 110 ± 33 nm, respectively, without substantially altering film thickness (550 ± 30 nm), phase, or morphology (Figure S7). The crystallite diameter could be made as small as ~30 nm by decreasing the annealing temperature and time to 475 °C and 15 min, respectively, again while maintaining phase purity (Figure S8). Our method for making nanoporous β-MVO films provides substantial flexibility to independently tune the film thickness and crystallite size, parameters that often play key roles in the performance of nanostructured photoelectrodes.

The optical absorptivity spectra and band gaps of the films were measured using an integrating sphere. Figure 2a shows the absorptivity spectra of films of different thicknesses grown on quartz substrates. We find an absorptivity of ~10^4 cm^{-1} at a

wavelength of 500 nm. The absorptance spectra were multiplied by the AM1.5G solar photon flux and integrated to obtain a maximum possible photocurrent density (J_{max}) and water-splitting efficiency ($\eta = \frac{1.23V \times J_{max}}{P_{AM1.5G}}$) of 2.6, 4.9, and 11.2 mA cm^{-2} and 3.2, 6.0, and 13.8% for the films with a thickness of 190, 460, and 990 nm, respectively (Figure 2b). Tauc-style plots of the absorptivity spectra suggest an indirect allowed band gap of 1.65−1.70 eV (Figure 2c), a direct forbidden gap of ~1.85 eV (Figure 2d), and a direct allowed gap of 2.25−2.30 eV (Figure 2e). These types of plots are useful mainly for giving an approximate optical band gap energy but cannot, in general, be relied on to decisively distinguish between direct/indirect or allowed/forbidden transitions, especially if such transitions are of similar energy or the material/sample is nonideal. The main conclusion from these data is that MVO has an optical band gap energy of 1.75 ± 0.1 eV. Yan et al. reported a direct band gap of 1.75 ± 0.1 eV based on diffuse reflectance data from a multiphase bulk powder.[5] The same authors concluded from density functional theory band structure calculations that β-MVO has a near-direct band gap, meaning that the indirect gap is smaller but within kT of the direct gap at room temperature, which is generally consistent with our results. Figure S9 compares the absorptivity spectra and Tauc fits of our β-MVO films on FTO-coated glass versus quartz substrates. The FTO-coated glass substrates absorb light in the ultraviolet and infrared (Figure S10), but they have little effect on the absorptance spectra of the MVO films, again showing that the β-MVO films grown on FTO-coated glass and quartz substrates are very similar.

2.2. PEC Performance. Aqueous PEC testing of the MVO films was performed unstirred in air using a three-electrode cell with both electrolyte−electrode (EE) and substrate−electrode (SE) illumination geometries (Figure 3a). According to the calculated Pourbaix diagram of ref 5, MVO is thermodynamically stable in a mild base (pH 8−10.5) within a 0.3 V window between the water redox potentials when the dissolved Mn and V ion concentrations are 10^{-4} mol kg^{-1}. We tested samples in several different electrolytes (Table 1) and found in all cases only extremely small photocurrents (~μA cm^{-2}) by constant-potential chronoamperometry under chopped 100 mW cm^{-2} AM1.5G simulated sunlight. Figure 3 shows representative current density versus potential ($J−E$) and current density versus time ($J−t$) data for our standard ~580 nm-thick β-MVO films in pH 9 borate buffer containing 0.1 M potassium iodide as a hole scavenger. $J−E$ sweeps at 50 mV/s showed small photocurrent (hundreds of μA cm^{-2}) at potentials >1 V versus RHE, but this photocurrent decayed under potentiostatic conditions to just a few μA cm^{-2} (Figure 3b,c). The dark current was also much smaller in $J−t$ than in $J−E$ measurements. The smaller currents obtained in the potentiostatic $J−t$ measurements indicate that the currents measured in the $J−E$ sweeps are influenced by transient processes such as charge trapping and interface charging. In contrast, nanostructured BiVO$_4$ films measured with the same setup and conditions produced much larger photocurrents (~0.66 mA cm^{-2} at 1.23 V vs RHE) and featured $J−E$ and $J−t$ data with self-consistent dark currents and photocurrents (Figure S11). These BVO control samples show that the transient $J−E$ behavior and very small photocurrent densities of the MVO films are caused by the samples, not the setup. Similarly tiny photocurrents were obtained for the oxidation of water and sulfite and the
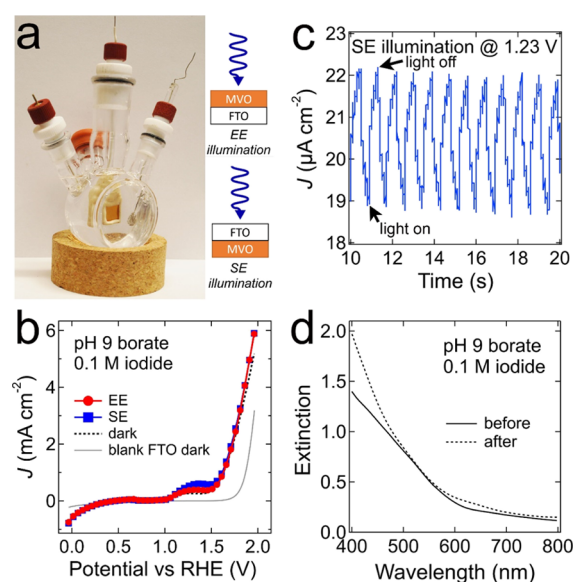

Figure 3. Aqueous PEC measurements. (a) Photograph of the PEC cell and schematics of the EE and SE illumination geometries. (b) Current density−potential ($J−E$) plots of a standard β-MVO film in pH 9 borate buffer with 0.1 M potassium iodide as a hole scavenger. $J−E$ data were collected at a scan rate of 50 mV/s using 1 sun AM 1.5G illumination. The small reversible wave at 1.3−1.4 V is due to the oxidation of Mn^{2+} to Mn^{3+} (Figure S12). Data for a blank FTO-coated glass substrate in the dark are also shown (gray line). (c) Current density−time ($J−t$) data acquired at 1.23 V vs RHE using chopped 1 sun illumination (1.25 Hz) in the SE geometry. We observe a very small photocurrent of ~3 μA cm^{-2}. (d) Optical extinction spectra of the film immediately before and after the PEC tests. See the Experimental Section for full experimental details, Figures S13−S16 for data in other electrolytes, and Figure S17 for PEC data of a blank FTO-glass substrate.

Table 1. Electrolyte Compositions Used in PEC Tests of Standard β-MVO Films[a]

electrolyte	hole/electron scavenger				
	no scavenger	KI	Na$_2$SO$_3$	NaIO$_3$	TBABr
pH 9 borate	√	√	√	√	
pH 9 phosphate	√	√	√	√	
pH 7 phosphate	√	√	√	√	
pH 13 (NaOH)	√	√	√		
acetonitrile					√

[a]These tests employed ~580 nm-thick films; the electrolytes did not contain added Mn or V.

reduction of water and iodate by MVO in all of the electrolytes listed in Table 1 (Figures S13−S16). Optical spectra showed that ~2/3 of these samples changed significantly during the PEC tests (e.g., Figure 3d), indicating that the MVO films were unstable under most of the conditions investigated here (vide infra).

We also tested MVO films of different thicknesses and average crystallite size to check whether the negligible photoresponse was specific to our standard ~580 nm-thick films. However, changing the film thickness (Figure S18), annealing time (Figure S19), or annealing temperature (Figure S20) did not meaningfully improve the photocurrent for iodide oxidation in borate electrolyte. While by no means exhaustive, this exploration of film parameters (Table S1) and electrolyte compositions (Table 1) demonstrates a general lack of
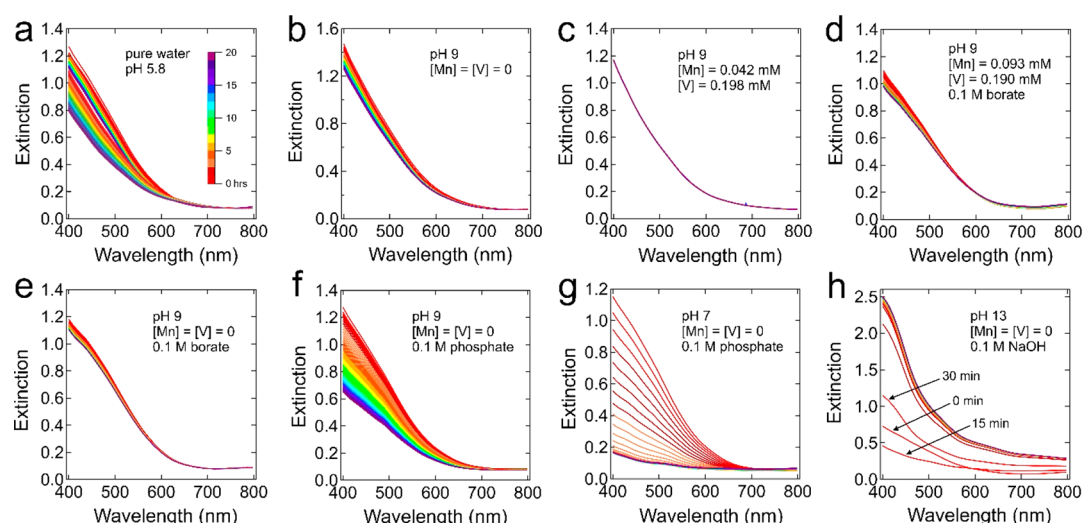
Figure 4. Chemical stability of MVO films in various aqueous solutions in the dark and without applied bias. Representative spectral time series for standard MVO films aged for 20 h in (a) pure water (pH 5.8), (b) pH 9 solution without added Mn and V, (c) pH 9 solution containing 0.042 ± 0.002 mM Mn and 0.198 ± 0.006 mM V, (d) pH 9 solution containing 0.093 ± 0.004 mM Mn, 0.190 ± 0.007 mM V and 0.1 M borate buffer, (e) pH 9 solution containing only 0.1 M borate buffer, (f) pH 9 solution containing only 0.1 M phosphate buffer, (g) pH 7 solution containing only 0.1 M phosphate buffer, and (h) 0.1 M NaOH (pH 13). Scans were acquired every 15 min for 20 h. After 20 h, the sample aged in pure water was transferred to a second vial of pure water and aged for another 20 h (double rainbow). See Figures S25−S27 for the corresponding photographs, SEM images, and XRD patterns for (e−g).

Table 2. XPS Elemental Quantification of Films Aged in Various Solutions for 20 h[a]

	atomic concentration (%)[b]					atomic ratio		
solution	Mn	V	O	C	P	Mn:V	O:Mn	Mn:P
none (control)	14.5	13.3	64.6	7.62		1.09	4.46	
water (pH 5.8)	18.0	10.5	62.9	8.60		1.71	3.49	
pH 9 borate	11.8	7.94	57.9	22.4		1.49	4.91	
pH 9 phosphate	11.2	4.33	67.5	9.65	7.33	2.59	6.03	1.53
pH 7 phosphate	12.6	0.229	65.2	6.54	15.4	55.0	5.18	0.82
pH 13 NaOH	23.3	0.466	67.9	8.36		50.0	2.91	

[a]Experiments employed ∼575 nm-thick β-MVO films; solutions did not contain added Mn or V. [b]Excluding Sn, K, and Na.

photoactivity from these β-MVO films. It is possible that MVO samples with significantly different composition (doping/alloying) and/or fabricated by a different method would show better photoactivity.

The absence of photocurrent from an illuminated semiconductor−electrolyte junction is typically caused by some combination of fast carrier recombination (bulk and/or surface) and fast photocorrosion (light-driven redox reactions that alter the electrode). We used postmortem optical extinction spectra to check for degradation of the films during the $J-E$ and $J-t$ measurements. Most of the films tested in pH 9 phosphate buffer showed negligible changes after PEC testing (Figure S14), suggesting that the films have short-term stability in this electrolyte and that the lack of photocurrent is due to fast recombination rather than photocorrosion in this case. In contrast, most of the films tested in the other electrolytes changed significantly during testing (Figures 3d, S13, S15, and S16). For example, the films in pH 7 phosphate electrolyte partially corroded during the measurements (Figure S15). However, as discussed in more detail in the next section, these changes occurred even in the dark without applied bias and were not strongly enhanced by illumination. A simple comparison of the total charge generated by light over the course of the PEC testing of each film (5−10 C cm^{-2}, calculated by integrating the product of the spectral photon

flux of the light source and the film absorptance and then multiplying this integral by the electron charge and illumination time) with the charge that would be required to completely photocorrode each film (∼0.065 C cm^{-2}, assuming two holes per formula unit of Mn$_2$V$_2$O$_7$) shows that at least 99% of the photogenerated carriers recombined instead of participating in local redox processes leading to photocorrosion. We conclude that the miniscule MVO photocurrent is the result of massive electron−hole recombination rather than photocorrosion.

Additional evidence that fast corrosion is not the main cause of the poor MVO photoresponse comes from PEC tests carried out in dry acetonitrile. Films measured in 0.1 M tetrabutylammonium bromide in acetonitrile were reasonably stable yet showed only μA cm^{-2} photocurrents (Figure S21), again implying that the photogenerated carriers are quantitatively lost to recombination. BVO electrodes measured under the same conditions produced photocurrents of ∼0.8 mA cm^{-2} in both illumination geometries (Figure S22).

2.3. Film Stability in Different Solutions. The chemical stability of the standard MVO films was assessed in several electrolytes using a combination of *in situ* optical extinction spectroscopy and postmortem XPS and SEM imaging. Figure 4a shows the behavior of an MVO film immersed in pure water (pH 5.8) in the dark for 20 h without applied bias or stirring.
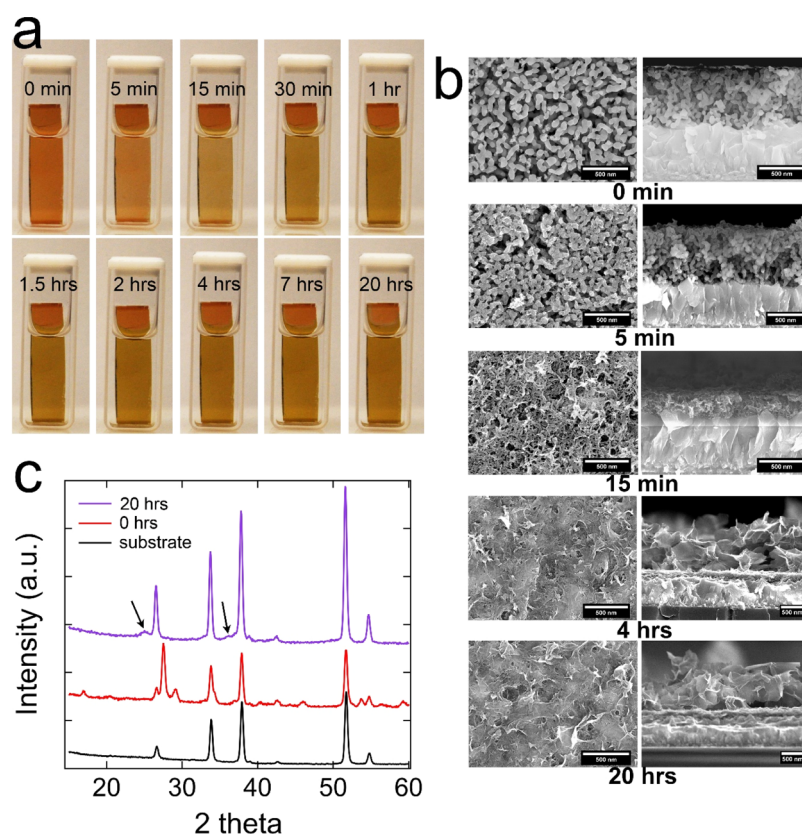
Figure 5. Chemical stability of MVO films in pH 13 NaOH solution in the absence of applied bias and light. (a) Photographic time series of a film from 0 min to 20 h of immersion in the solution. The immersed part of the film begins to change color within seconds and stabilizes with a distinct brownish hue after ~1 h. (b) Plan-view and cross-sectional SEM images of films aged in solution for 0 min, 5 min, 15 min, 4 h, and 20 h. Each white scale bar is 500 nm. (c) XRD patterns of an MVO film before immersion (red) and after 20 h of immersion (purple). The pattern of a clean FTO-coated glass substrate is also shown (black). The pattern of the aged film shows a complete loss of MVO peaks and the appearance of weak, broad peaks at 25.0 and 36.2° (labeled with arrows). The peak at 25.0° may be due to MnO(OH) (PDF # 01-088-0649), while the peak at 36.2 may be due to Mn_3O_4 (PDF # 00-001-1127). All patterns were acquired with an angle of incidence of 0.5°.

We see that the film extinction decreased monotonically with time and nearly stabilized by the end of the experiment at ~85% of its initial value. The corresponding XP spectra showed an increase in the Mn/V ratio from 1.09 to 1.71, indicating preferential loss of surface vanadium upon aging in water (Figure S23 and Table 2). In principle, these changes can be explained by either partial dissolution of the MVO film to form a saturated solution of Mn and V species or the self-limited growth of a surface corrosion layer. To distinguish between these two possibilities, we transferred the aged film to a vial of fresh water and found that the decrease in optical extinction resumed (Figure 4a). These results are consistent with dissolution of β-MVO in water, and not with self-passivated corrosion of MVO to form a stable manganese-rich surface layer. In a sufficient volume of water, the films would likely fully dissolve within days.

We next evaluated the stability of our films within the purported stability field of β-MVO reported in ref 5. The electrolyte was a saturated aqueous solution of Mn and V at pH 9 made by completely dissolving an MVO film in 1 mM HCl, increasing the pH to 9 with NaOH, and removing the resulting precipitate by centrifugation. The Mn and V concentrations were measured by ICP-MS to be 0.042 ± 0.002 mM and 0.198 ± 0.006 mM, respectively. Films aged in this electrolyte for 20 h exhibited completely stable extinction spectra (Figure 4c), indicating that MVO may be thermodynamically stable under these conditions, as predicted by the

calculated Pourbaix diagram of ref 5. The presence of dissolved Mn and V species is essential for the observed stability. Films aged in pH 9 solution without added Mn and V were not stable (Figure 4b). We also found that the addition of other ions to the Mn- and V-saturated pH 9 solution (*e.g.*, 0.1 M borate, 0.1 M NaCl, or 0.1 M KI) destabilized the films (Figures 4d and S24). Unfortunately, the use of Mn- and V-saturated pH 9 electrolytes did not improve the photocurrent for iodide oxidation, which remained at only ~μA cm⁻² levels (Figure S24).

Dark stability tests performed in the buffered electrolytes used for the PEC measurements in Figures 3 and S13−S15 (no added Mn or V) show that MVO stability increased in borate buffer and decreased in phosphate buffer compared to unbuffered solution at the same pH (Figure 4e,f). Films aged for 20 h in 0.1 M borate buffer at pH 9 showed a moderate increase in the Mn/V ratio by XPS (from 1.09 to 1.49) and slight surface etching of the MVO crystallites but no major changes in optical extinction, morphology, or phase (Table 2 and Figures S23 and S25). This increased stability may result from borate anions binding to cations on the MVO surface and slowing surface corrosion. However, increasing the borate concentration from 0.1 to 1 M only decreased film stability (Figure S28). We speculate that the concentration-dependent speciation of polyborate ions (*i.e.*, $[B(OH)_4]^-$, $[B_2(OH)_7]^-$, $[B_3O_3(OH)_4]^-$, $[B_4O_5(OH)_4]^{2-}$, *etc.*) may be responsible for the loss of MVO stability at higher borate concentrations.[30] In
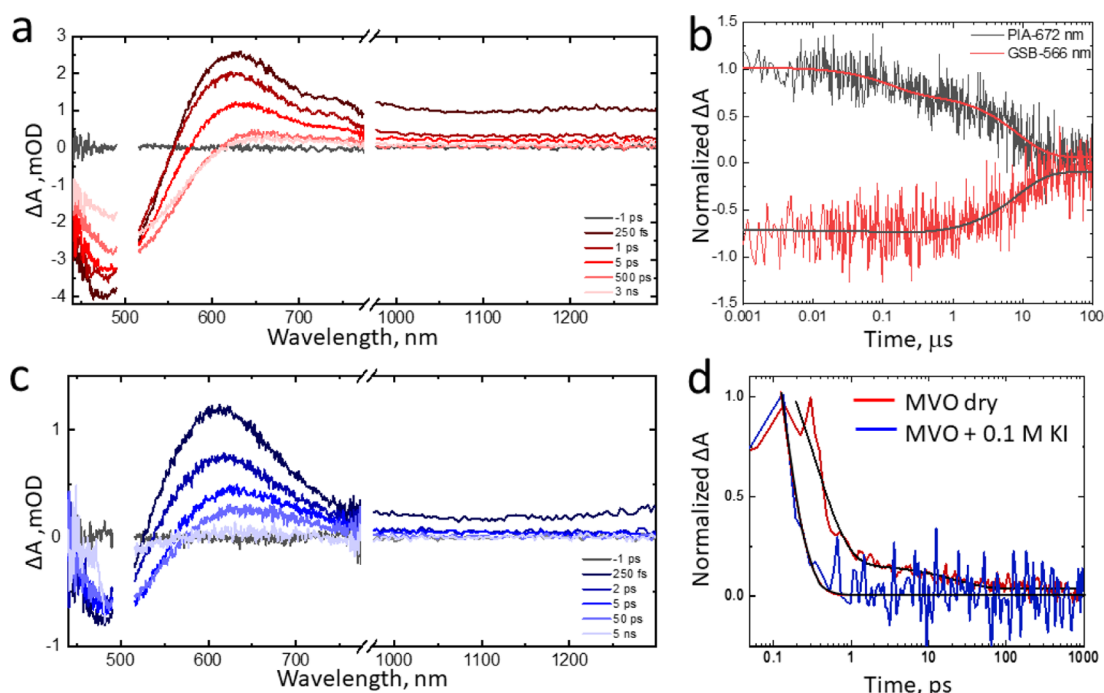
Figure 6. TA spectra. TA spectra in the visible and near-infrared regions at various delay times after 500 nm excitation of a (a) dry β-MVO film and (c) β-MVO film immersed in 0.1 M aqueous borate buffer at pH 9. (b) Kinetics of the bleach and photoinduced absorption (PIA) decay at representative wavelengths on the ns–μs timescales for the dry film. (d) Near-IR (NIR) decay kinetics and fits (1100 nm probe) for a dry film and a film immersed in pH 9 borate buffer solution containing 0.1 M KI hole scavenger.

contrast to borate buffer, films aged in phosphate buffer dramatically degraded to form a dense layer of amorphous manganese phosphates and manganese oxides, with the degradation significantly faster at pH 7 than pH 9 (Table 2 and Figures 4g, S23, S26, and S27).

Overall, we find that β-MVO is unstable in water even in the absence of light and applied bias. It dissolves or corrodes in both pure water and at pH 9. The corrosion is slowed in dilute borate buffer and accelerated in concentrated borate buffer. Phosphate converts MVO to other compounds. We found that the addition of 0.1 M NaCl, NaClO$_4$, or K$_2$SO$_4$ to water at pH 9 also reduced the stability of the films (not shown). MVO does appear to be stable in Mn- and V-saturated water at pH 9, but this stability is lost upon the addition of supporting electrolytes or hole scavengers, and only tiny photocurrents are obtained in Mn- and V-saturated electrolytes. The stability of the films further decreases under applied bias and illumination (e.g., compare Figures 3d and 4e). In addition to their near lack of photoactivity, the poor stability of these native, nano-structured β-Mn$_2$V$_2$O$_7$ films makes them an unlikely candidate for practical solar water splitting.

We also tested dark stability in two nonaqueous solvents, ethanol and acetonitrile. Films in ethanol exhibited some initial minor changes in extinction that stopped within a few hours, while films in acetonitrile had completely stable extinction spectra over the entire 20 h aging tests (Figure S29). PEC testing in acetonitrile resulted in a small change (increase) in extinction but only μA cm^{-2} photocurrents (Figure S21), consistent with quantitative electron–hole recombination.

2.4. Behavior of β-MVO Films at pH 13. The performance of OER photoanodes in strong base (pH $\geq$ 13) is important because resistance losses are low and many OER catalysts work best at high pH.[31] Ref 5 stated that MVO is thermodynamically unstable in strong base and should

decompose to Mn$_x$O$_y$ and soluble vanadium oxyanions. Regardless, these authors reported that a film of composition Mn$_{0.5}$V$_{0.5}$O$_x$ placed in 0.1 M NaOH solution (pH 13) with 0.05 M [Fe(CN)$_6$]$^{3-/4-}$ redox couple produced a stable anodic photocurrent of ~0.1 mA cm^{-2} under chopped 385 nm illumination. Repeating the measurement on a duplicate sample with 0.1 M NaOH and without the facile redox couple yielded no measureable photocurrent.[5] Based solely on these photocurrent data and without characterizing film phase purity or elemental composition, the authors concluded that β-MVO is kinetically stable under illumination at pH 13. PEC stability of MVO in concentrated base at the OER potential would be surprising and encouraging for water splitting applications. However, the lack of proof of phase and elemental composition calls into question whether the samples measured in ref 5 were in fact MVO rather than some other phase(s).

Our stability tests at pH 13 show that β-MVO films rapidly degrade to form amorphous manganese oxides and hydroxides. This degradation occurred regardless of illumination or the presence of the [Fe(CN)$_6$]$^{3-/4-}$ redox couple (0.05 M). We found no evidence for significant kinetic stability of β-MVO in concentrated base. Optical spectra show that the film extinction first dramatically decreased within seconds and minutes and then rapidly increased and stabilized within ~1 h to a new spectrum with extinction values ~2× higher than those of the initial MVO film (Figure 4h). These optical changes were also apparent in photographic time series (Figure 5a). SEM time series show that the films rapidly (~1 h) convert into an ~800 nm-thick, porous layer of interconnected, crumpled nanoscale sheets sitting on an ~200 nm-thick, much denser interlayer on the FTO (Figure 5b). Films aged for 20 h were nearly amorphous by XRD (Figure 5c), with the MVO peaks replaced by weak, broad peaks at 25.0 and 36.2° that may be due to MnO(OH) (PDF # 01-088-0649) and Mn$_3$O$_4$

Table 3. Fitting Parameters for GSB (520 nm) and Visible PIA (715 nm) for dry and Electrolyte-Immersed β-MVO Films[a]

	dry		0.1 M borate (pH 9)		buffer + 0.1 M KI		buffer + 0.1 M NaIO$_3$	
	520 nm	715 nm	520 nm	715 nm	520 nm	715 nm	520 nm	715 nm
A$_1$	16%	48%	57%	65%	68%	68%	53%	64%
t_1 (ps)	262 (157)	0.48 (0.04)	106 (18)	3.65 (0.5)	257 (37)	2.0 (0.1)	79 (21)	1.6 (0.2)
A$_2$	14%	33%	43%	35%	32%	32%	47%	36%
t_2 (ps)	3135 (1289)	7.7 (0.53)	828 (129)	582 (80)	1971 (1164)	478 (40)	671 (146)	128 (15)
A$_3$	70%	19%						
t_3 (ps)	>10000	7197 (633)						

[a]Fit uncertainties are given in parentheses.

(PDF # 00-001-1127), respectively. Films immersed in pH 13 for even 5 min were amorphous by XRD (Figure S30). Meanwhile, XPS of the 20 h films showed nearly complete loss of vanadium, a Mn 3s peak separation consistent with Mn^{4+}, and a sharp oxygen peak at 529.9 eV with weak high-energy features that we assign to the bulk oxygen of MnO$_2$ and surface hydroxides (Figure S23), consistent with the O/Mn atomic ratio of 2.91 in Table 2. These data indicate that β-MVO films at pH 13 quickly degrade to manganese oxides and hydroxides. There was some hope that a self-passivating layer of MnO$_x$ would form on the MVO surface, protecting it from bulk corrosion and acting as a reasonable water oxidation catalyst, but this appears not to happen. We conclude that the samples tested at pH 13 in ref 5 were probably not MVO but rather some mixture of Mn$_x$O$_y$(OH)$_z$ decomposition products.

Unfortunately, $J-E$ and $J-t$ measurements of films in 0.1 M NaOH showed nearly zero photocurrent (μA cm^{-2} or less) for the oxidation of [Fe(CN)$_6$]$^{4-}$, iodide, sulfite, or water at any time during the 20 h aging experiments (Figures S31 and S16). Given the extreme instability of β-MVO at this pH, we can only speculate that the photocurrent reported in ref 5 for [Fe(CN)$_6$]$^{4-}$ oxidation originated from some unique phase mixture produced by the degradation of these "Mn$_{0.5}$V$_{0.5}$O$_x$" films in strong base. It is also possible, although we believe less likely, that the particular composition or microstructure of these films imbued them with better stability and photoactivity than the nanostructured β-MVO films explored here.

2.5. Femtosecond TAS. The hypothesis that fast recombination contributes to the poor PEC performance of the MVO films was tested using visible, near-IR (NIR), and mid-IR femtosecond TAS. For all MVO films and all conditions investigated, a ground-state bleach (GSB) centered at 475−500 nm and a broad photoinduced absorption (PIA) centered at 600−625 nm arose within the instrument response time after photoexcitation at 500 nm (Figure 6a). For dry samples, about half of the initial amplitude of the visible PIA was lost with a sub-ps time constant, with additional slower decays of 7 ps (30%) and 7 ns (20%) (see Table 3 for a full list of fitted time constants). A small portion (<20%) of the PIA signal persisted beyond the 10 ns timescale, decaying with time constants of 128 ns and 8.6 μs (Figure 6b). We note that the decay kinetics were not strongly power-dependent. The rapid decay of the PIA also occurred with a red shift, which uncovers additional GSB at 550 nm that does not decay significantly within the course of 5 ns. Due to peak shifting, it is difficult to judge the relative amplitudes of fast versus slow GSB decay, but the long-lived bleach could comprise up to 70% of the total signal. In the NIR, there is a broad PIA spanning the entire spectral window that decays to 25% of its initial amplitude by 5 ps and completely by ∼0.5 ns (Figure 6a). There was no substantive change in dynamics with or without air exposure.

The mid-IR PIA dynamics lack the ps-scale initial decay, instead possessing ∼200 ps and ∼1 ns decay components (Figure S32 and Table S2). Mid-IR kinetics could not be probed at delay times greater than 5 ns due to instrument limitations or in the presence of electrolytes due to strong absorption by the solvent in the infrared region.

TA spectra collected in the visible and NIR for films immersed in a 0.1 M aqueous borate buffer solution at pH 9 under the same excitation conditions as the dry films (λ_{pump} = 500 nm) reveal a significant quenching of the long-lived (>0.5 ns) GSB and complete quenching of NIR PIA signals beyond a few ps, as compared to dry films, while the faster decays are mostly unaffected (Figure 6c). We found that adding a hole scavenger (0.1 M KI) to the borate buffer accelerates the decay of the NIR PIA (Figures 6d and S33a) such that all signal is lost within 1 ps, whereas some long-lived GSB remains. Adding an electron scavenger (0.1 M NaIO$_3$) to the buffer solution had the same effect as the buffer alone, significantly reducing the >0.5 ns component but not altering the faster decay components (Figure S33b).

Prior work on BVO provides some guidance about the likely origin of the TA signals in MVO.[32,33] The sub-ps PIA features in the visible region are initially blue-shifted from the band edge, likely resulting from band gap renormalization and related screening effects that temporarily shift and broaden spectral features shortly after photoexcitation. As charge carriers relax on a ps time scale, these contributions diminish. Although it is tempting to assign the persistent GSB and associated strong PIA peaking around 650 nm (Figure 6a,b) to long-lived free charge carriers, we believe that other factors account for most, if not all, of this signal. One contribution is thermally induced absorption change, which manifests as a derivative-like spectral feature near the band edge that decays over microseconds after laser excitation by heat dissipation to the surroundings. Variable-temperature steady-state difference spectra, Figure S34, reveal a close match with the TA spectra at long delay times (dashed red curve in Figure S35). We note that an increase in temperature of only a few degrees could produce the roughly 1 mOD of long-lived GSB observed for the dry films, consistent with the predicted temperature increase.[33]

A second contribution to the TAS signal is transient reflectivity (TR) that results from a change in refractive index upon photoexcitation and produces a derivative-like spectral contribution similar to the effect that transient heating has on absorption. Although signals were too weak to be quantitatively analyzed, TR spectral features and their associated kinetics overlap strongly with GSB and visible PIA from TAS (Figure S35). The relative contributions of the TR and thermal effects are difficult to disentangle, given their similar spectral profiles. The addition of the borate buffer solution ameliorates[a]

the thermal effect by reducing the temperature increase in the film through the solvent heat capacity and thus effectively eliminates the residual PIA and GSB on μs timescales (Table 3). The TR contribution is also reduced upon buffer addition through improved index matching between the film and solvent compared with gaseous N_2.[34] Therefore, the TAS data for MVO films immersed in electrolyte, which possess no GSB signal beyond a few ns, more accurately reflect the true excited state population dynamics than does TAS on the dry MVO films.

Additional evidence against the existence of long-lived free holes is found in the PIA spectral features far from the MVO band edge (>800 nm), which are not influenced by the thermal effect or TR signals. This portion of the NIR spectrum does not possess the long-lived decay component present near the band edge, and the addition of the KI hole scavenger further reduces the decay time to <1 ps (Figure 6d and Table S3). This behavior concurs with the prior assignment of NIR PIA features in BVO to hole absorption and further suggests that scavenging with KI markedly accelerates loss of the hole population.[35] The mid-IR TA, although undoubtedly associated with free carriers, cannot be a priori assigned to electron or hole absorption due to our inability to make mid-IR measurements in the presence of a scavenger. Nevertheless, the lack of a sub-ps decay compared with the NIR kinetics implies that the opposite carriers (*i.e.*, electrons) are responsible for the mid-IR absorption. As such, we infer that electrons undergo slower trapping kinetics than holes, including up to one-third of the electron population remaining as free carriers with lifetimes >1 ns. The residual GSB with a lifetime >1 ns also represents roughly one-third of the total amplitude (Figure S36b), which likely reflects the band filling contribution of the free electrons detected in mid-IR TAS. The amplitude of this long-lived GSB increases further when the hole scavenger KI is introduced, suggesting that faster separation of holes from free electrons reduces recombination.

We note that the faster NIR decay in the presence of the KI hole scavenger shows that photogenerated holes reach the MVO surface. We can conclude that (1) the hole diffusion length is not extremely short and (2) the miniscule photocurrents observed in our PEC tests are caused mainly by fast surface trapping and recombination. Surface recombination seems to be the major loss channel for holes in these MVO films.

One possible mechanism for efficient surface recombination could reside in reduced vanadium sites below the conduction band edge. Oxygen vacancies are known to be thermodynamically stable defects in many oxides, and if the energetics enable electron localization at proximal vanadium sites, holes may preferentially become trapped at the reduced vanadium species. In particular, if such species reside on the MVO surface, efficient surface recombination could result. Unlike in $BiVO_4$,[36] no clear spectroscopic evidence for such states was found in MVO, although the optical transition energies and strengths may be significantly altered in MVO and thus outside the range of investigation or obscured by other features. Thus, vacancies may play a role in excited state dynamics in analogy with $BiVO_4$, but a definitive assignment for MVO is not yet possible. Further investigation of the role of vacancy-related trapping and recombination is warranted.

The scenario presented here for MVO is less favorable for water oxidation than BVO, for which comprehensive TAS analysis has shown that a significant fraction of free holes persists to the ns time scale, while electrons are quickly trapped. Common experimental artifacts present near the band edge initially clouded our interpretation, but probing in the presence of electrolytes and in the NIR provides clarity that the free hole population is exceedingly fleeting due to a combination of bulk and surface trapping and recombination. Mid-IR probing reveals the existence of a significant free electron population with distributed decay times between 100 ps and 1 ns. We tried to further support these conclusions with steady-state spectroelectrochemistry of films in the borate electrolyte, but the resulting difference spectra showed only very broad and irreversible features that proved unhelpful in better understanding the TA results.

3. CONCLUSIONS

We evaluated the stability and PEC performance of nanostructured β-$Mn_2V_2O_7$ films made by calcination of a spin-cast molecular ink. β-MVO was found to dissolve in pure water and corrode in neutral and alkaline aqueous electrolytes even in the absence of light and applied bias. At pH 13, it corrodes within minutes to form amorphous manganese (hydr)oxides. While β-MVO appears to be stable in saturated solutions of Mn and V at pH 9, this stability is lost upon the addition of other ions, including supporting electrolytes, buffers, and hole scavengers. The extreme instability of β-MVO in water presents a major challenge to its use in water splitting devices.

In addition to poor stability, the β-MVO films showed extremely small photocurrents (<3 μA cm^{-2}, equivalent to an overall external quantum efficiency of <0.05%) for the oxidation of iodide, sulfite, bromide, and water and the reduction of iodate and water in all of the aqueous and nonaqueous electrolytes that we tested. Comparison of postmortem optical extinction spectra with the photogenerated (but uncollected) charge and the charge needed for complete corrosion of the tested films shows that photocorrosion cannot account for this lack of photocurrent. Instead, the β-MVO films must suffer from some mix of massive bulk recombination (*i.e.*, an ultrashort carrier diffusion length) and a high surface recombination velocity (*i.e.*, fast electron–hole recombination at the MVO surface). Femtosecond TA spectra show that the vast majority of photogenerated holes are trapped within a few picoseconds and recombine with free electrons on timescales of up to a few nanoseconds. The short hole lifetime ($\tau_h \sim 50$ ps for films immersed in borate buffer) may result in a very short hole diffusion length (<5 nm) that severely limits the photocurrent of our films despite their nanostructured morphology. However, the markedly faster TA decay kinetics of films immersed in electrolyte containing a hole scavenger indicate that most photogenerated carriers do reach the MVO surface, pointing to fast surface recombination as the main reason for the miniscule photocurrents generated by these samples. Coating the β-MVO surface with a passivating, protective, and catalytic layer may boost the photoactivity and stability of this material enough to justify further study of its potential for solar water splitting.

4. EXPERIMENTAL SECTION

4.1. Materials. All chemicals were used as received unless otherwise noted. Water (18.2 MΩ, Millipore Milli-Q Gradient) was used in all experiments. Fused quartz substrates and quartz tubes were purchased from GM Associates, Inc. FTO-coated glass substrates (TEC 8, Pilkington) were purchased from Hartford Glass Company. Hellmanex III detergent, manganese acetate tetrahydrate (>99.99%),

K_2SO_4 (99%), acetonitrile (>99.8%), and NaOH (99.99%) were purchased from Sigma Aldrich. Vanadyl acetylacetonate (>99%) was purchased from Acros Organics. Poly(ethylene glycol)-*block*-poly-(propylene glycol)-*block*-poly(ethylene glycol) Pluronic F-108 (average M_n ~ 14,600, 82.5 wt % PEG) was purchased from Aldrich. KH_2PO_4 (>99.0%) was purchased from Sigma Life Sciences. Potassium ferrocyanide (>99.3%), $NaIO_3$ (99.0%), Na_2SO_3 (98.2%), and isopropyl alcohol (99.9%) were purchased from Fisher Scientific. TraceMetal grade nitric acid for ICP-MS measurements was purchased from Fisher chemicals. Potassium ferricyanide (>99.9%) was purchased from J.T. Baker Chemical company. Ethylene glycol (>99%) and concentrated nitric acid (for the MVO inks) were purchased from Macron Fine Chemicals. KI (99.9%) was purchased from Alfa Aesar. Boric acid (reagent grade) was purchased from Ward's Science. Tetrabutylammonium bromide (>99%) was purchased from TCI. Silver paint (Leitsilber 200) was purchased from Ted Pella. Loctite 9462 epoxy was purchased from McMaster-Carr. Ag/AgCl (4 M KCl), and nonaqueous Ag/Ag^+ reference electrodes were purchased from CH Instruments.

4.2. Film Fabrication. All procedures were carried out in air. Fused quartz and FTO-coated glass substrates were cleaned by sequential sonication in an aqueous solution of Hellmanex III detergent (5% v/v), pure water, and isopropyl alcohol (15 min each). After sonication, the substrates were dried in a furnace at 110 °C for 1 h. Molecular inks for spin coating were prepared by adding $VO(acac)_2$ (1 mmol, 0.265 g) followed by dropwise addition of concentrated nitric acid (0.32 g) to a mixture of ethylene glycol and water (1.5 g each). The mixture was sonicated for 5 min to completely dissolve the vanadium salt. Next, $Mn(CH_3COO)_2 \cdot 4H_2O$ (1 mmol, 0.245 g) was added to the solution and sonicated until a clear bluish-green solution was obtained, to which the triblock copolymer Pluronic F-108 (0.4 g) was added as a structure-directing and thickening agent for making porous MVO films. The solution was sonicated for an additional 3 h to obtain a dark blue-green viscous ink for spin coating. Our standard films were spin cast at 2000 rpm for 20 s followed by 3000 rpm for 40 s. After drying, the films were annealed at 500 °C for 30 min using a 10 °C min^{-1} heating rate and then cooled naturally to room temperature. This procedure yielded nanostructured β-MVO films with a thickness of ~575 nm and an average crystallite diameter of ~53 nm.

4.3. Physical Characterization. Grazing-incidence XRD patterns were obtained on a Rigaku SmartLab diffractometer (Cu Kα radiation) at room temperature. Unless otherwise stated, the angle of incidence (ω) was selected to maximize the intensity of the 111 reflection of β-MVO at $2\theta = 27.5°$. Synchrotron powder XRD was performed on beamline 11 of the Advanced Photon Source (APS), Argonne National Laboratory using an X-ray wavelength of 0.458092 Å, a step size of 0.001°, and a scan speed of 0.01°/s. SEM was performed on an FEI Magellan 400L XHR SEM instrument operating at 10 kV with a 13 pA beam current. Low-conductivity samples were sputtered with 1 nm of iridium prior to imaging. Raman spectra were obtained using a Renishaw inVia confocal Raman microscope with a 50× objective lens and $\lambda_{incident}$ = 532 nm at 1% power and a 60 s acquisition time. The Mn and V content of the MVO films and electrolyte solutions was quantified by ICP-MS using a ThermoFisher Scientific iCAP RQ C2 inductively coupled plasma mass spectrometer. IV-ICPMS-71A (Inorganic Ventures) was used as the calibration standard. MVO films were dissolved in nitric acid (10%) for elemental analysis. Dissolved film solution was diluted 100 times with 1% nitric acid before measurement. The Mn- and V-containing electrolyte samples were made by dissolving an MVO film in 1% nitric acid, increasing the pH to 9.0 using aqueous NaOH, centrifuging the resulting suspension to remove precipitates, and diluting the mother liquor 100-fold with 1% nitric acid prior to ICP-MS measurements.

4.4. Optical Characterization. Room-temperature optical measurements to determine the absorptance spectra and band gap of the MVO films were performed on a PerkinElmer Lambda 950 spectrophotometer equipped with a 60 mm integrating sphere. Variable-temperature data were acquired by placing films grown on sapphire substrates (Edmund Optics) in a Janis ST-100 cryostat

mounted in the spectrophotometer. For sample stability tests, films grown on FTO-coated glass substrates were placed in electrolyte-filled cuvettes, and their extinction spectra were measured at 15 min intervals for 20 h.

4.5. X-ray Photoemission Spectroscopy. X-ray photoemission spectra were acquired on a Kratos AXIS Supra spectrometer using monochromatic Al Kα radiation (1487 eV). Survey and high-resolution core-level spectra were collected at 160 and 20 eV pass energies, respectively. All spectra were charge-corrected using the C 1s peak of adventitious carbon at 184.8 eV. Relative atomic compositions were calculated by integrating the Mn $2p_{3/2}$, O 1s, C 1s, and V $2p_{3/2}$ peaks in CasaXPS using its library of relative sensitivity factors. For stability studies, MVO films on FTO-coated glass substrates were immersed in the electrolyte of interest for 20 h, briefly doused with water, and dried with a nitrogen gun.

4.6. PEC Measurements. Three-electrode measurements were performed in a four-neck electrochemical cell fitted with a quartz window. Working electrodes were prepared from films by affixing a long wire to a bare region of the FTO-coated glass substrate using silver paint, threading the wire through a hollow quartz tube, and mounting the sample to the end of the tube with epoxy. The epoxy encased the entire substrate except a square-shaped area of 1−1.4 cm^2 exposed to the solution. Biased three-electrode measurements used a Ag/AgCl (4 M KCl) reference electrode and a platinum mesh counter electrode. The primary aqueous electrolytes used were phosphate buffer (0.1 M, pH 7), phosphate buffer (0.1 M, pH 9), borate buffer (0.1 M, pH 9), and NaOH solution (0.1 M, pH 13). The use of supporting electrolytes was avoided due to their negative impact on β-MVO stability. KI (0.1 M) and Na_2SO_3 (0.1 M) were used as hole scavengers, and $NaIO_3$ (0.1 M) was used as an electron scavenger. Electrolyte conditions from ref 5 were recreated with NaOH (0.1 M) and $[Fe(CN)_6]^{4-/3-}$ (50 mM) as a facile redox couple. Nonaqueous photoelectrochemistry was carried out in acetonitrile containing TBABr (0.1 M) as an electrolyte and hole scavenger.

$J-E$ measurements utilized a PalmSens electrochemical interface controlled by PSTrace 5.7. A Newport 91160 Class A solar simulator fitted with a 300 W xenon arc lamp and an AM 1.5G filter was used as a light source. The power density at the sample position was measured with a pyroelectric radiometer (RkP-575 power probe and Rk-5710 power meter, Laser Probe, Inc). The absolute spectral irradiance of the solar simulator was measured using a USB4000 spectrometer (Ocean Optics) and a calibrated light source (HL-2000-Cal, Ocean Optics). $J-E$ measurements were performed using linear sweep voltammetry (LSV) in the dark and under 1 sun illumination incident from either the electrolyte (EE illumination) or substrate (SE illumination). Five cyclic voltammetry (CV) scans were performed immediately prior to each LSV scan to ensure stable electrochemical behavior under each measurement condition. The potential range was −0.1 V to 2.0 V for anodic scans and 0.2 V to −1.0 V for cathodic scans, with a scan rate of 50 mV/s for both CV and LSV experiments. $J-t$ measurements were carried out at a constant potential of 1.23 V versus RHE for oxidation reactions and −0.6 V versus RHE for reduction reactions using 1 sun SE illumination chopped at 1.25 Hz.

4.7. Transient Absorption Spectroscopy. Ultrafast TA measurements were carried out using a Coherent Libra Ti/Sapphire laser with a 1 kHz, 800 nm output (150 fs pulse width) in a pump−probe configuration. The 500 nm pump pulse was generated with a TOPAS-C optical parametric amplifier. Visible (λ_{probe} = 440−800 nm) and NIR probe (λ_{probe} = 750−1600 nm) pulses were generated by focusing a portion of the 800 nm fundamental into a thin or thick sapphire window, respectively. A portion of the probe was picked off before reaching the sample as a reference to increase signal-to-noise ratio. The time between the pump and probe was controlled using a mechanical delay stage, and data were collected using the Helios software package from Ultrafast Systems. Data were chirp-corrected and analyzed using SurfaceXplorer from Ultrafast Systems. A second TOPAS-C optical parametric amplifier was used to generate ~150 fs 3500−4500 nm probe pulses for mid-IR TAS. The spectrally dispersed probe was detected with liquid nitrogen-cooled HgCdTe array detectors.

Nanosecond–microsecond (1 ns–400 μs) TA measurements (EOS, Ultrafast Systems) were collected using the same pump pulse as the ultrafast measurements. The probe pulse was produced in a diode-laser pumped photonic crystal fiber and electronically delayed relative to the pump pulse with a digital delay generator.

A comparison of repeated measurements was used to verify that the TA data were dominated by reversible photophysics and have insignificant contributions from sample degradation.

■ ASSOCIATED CONTENT

Ⓢ Supporting Information

The Supporting Information is available free of charge at https://pubs.acs.org/doi/10.1021/acs.chemmater.1c02065.

Experimental results including structural characterization of samples grown on quartz substrates, Raman spectra, XRD and SEM data for films of different thicknesses and crystallite sizes, X-ray photoelectron spectra, optical data, PEC data in different electrolytes, film degradation studies, TA spectra and kinetics under different conditions, and steady-state variable-temperature optical difference spectra (PDF)

■ AUTHOR INFORMATION

Corresponding Author

Matt Law − *Department of Chemistry and Department of Chemical Engineering and Materials Science, University of California, Irvine, California 92617, United States;* ⓞ orcid.org/0000-0001-7645-9908; Email: lawm@uci.edu

Authors

Yash Gargasya − *Department of Chemistry, University of California, Irvine, California 92617, United States;* ⓞ orcid.org/0000-0003-0324-090X

Melissa K. Gish − *National Renewable Energy Laboratory, Golden, Colorado 80401, United States;* ⓞ orcid.org/0000-0002-9886-3626

Vineet V. Nair − *Department of Chemical Engineering and Materials Science, University of California, Irvine, California 92617, United States*

Justin C. Johnson − *National Renewable Energy Laboratory, Golden, Colorado 80401, United States;* ⓞ orcid.org/0000-0002-8874-6637

Complete contact information is available at:
https://pubs.acs.org/10.1021/acs.chemmater.1c02065

Author Contributions

Y.G. carried out the thin-film fabrication, characterization, PEC measurements, and stability studies. M.K.G. and J.C.J. performed the TA measurements and analysis. M.L. directed the research. Y.G., J.C.J., and M.L. wrote the manuscript with the input from all authors. All authors have given approval to the final version of the manuscript.

Notes

The authors declare no competing financial interest.

■ ACKNOWLEDGMENTS

■ REFERENCES

(1) Montoya, J. H.; Seitz, L. C.; Chakthranont, P.; Vojvodic, A.; Jaramillo, T. F.; Nørskov, J. K. Materials for solar fuels and chemicals. *Nat. Mater.* **2017**, *16*, 70−81.

(2) Abdi, F. F.; Berglund, S. P. Recent Developments in complex metal oxide photoelectrodes. *J. Phys. D: Appl. Phys.* **2017**, *50*, 193002−193025.

(3) Zhou, L.; Shinde, A.; Guevarra, D.; Haber, J. A.; Persson, K. A.; Neaton, J. B.; Gregoire, J. M. Successes and opportunities for discovery of metal oxide photoanodes for solar fuels generators. *ACS Energy Lett.* **2020**, *5*, 1413−1421.

(4) Fountaine, K. T.; Lewerenz, H. J.; Atwater, H. A. Efficiency limits for photoelectrochemical water splitting. *Nat. Commun.* **2016**, *7*, 13706−13715.

(5) Yan, Q.; Li, G.; Newhouse, P. F.; Yu, J.; Persson, K. A.; Gregoire, J. M.; Neaton, J. B. $Mn_2V_2O_7$: An earth abundant light absorber for solar water splitting. *Adv. Energy Mater.* **2015**, *5*, 1401840−1401846.

(6) Skorupska, K.; Parkinson, B. A. Combinatorial synthesis and screening of oxide materials for photoelectrochemical energy conversion. In *Photoelectrochemical Solar Fuel Production: From Basic Principles to Advanced Devices*; Giménez, S., Bisquert, J., Eds.; Springer: Cham, Berlin, 2016; pp. 427−462.

(7) Ninova, S.; Strach, M.; Buonsanti, R.; Aschauer, U. Suitability of Cu-substituted β-$Mn_2V_2O_7$ and Mn-Substituted β-$Cu_2V_2O_7$ for photocatalytic water-splitting. *J. Chem. Phys.* **2020**, *153*, 084704.

(8) Zhou, L.; Shinde, A.; Guevarra, D.; Richter, M. H.; Stein, H. S.; Wang, Y.; Newhouse, P. F.; Persson, K. A.; Gregoire, J. M. Combinatorial screening yields discovery of 29 metal oxide photo-anodes for solar fuel generation. *J. Mater. Chem. A* **2020**, *8*, 4239−4243.

(9) Seenivasan, S.; Moon, H.; Kim, D. H. Investigation of bulk carrier diffusion dynamics using β-$Mn_2V_{2-x}Mo_xO_7$ photoanodes in solar water splitting. *Appl. Surf. Sci.* **2021**, *540*, 148376−148387.

(10) Liao, J.-H.; Leroux, F.; Piffard, Y.; Guyomard, D.; Payen, C. Synthesis, structures, magnetic properties, and phase transition of manganese(II) divanadate: $Mn_2V_2O_7$. *J. Solid State Chem.* **1996**, *121*, 214−224.

(11) Sannigrahi, J.; Giri, S.; Majumdar, S. Magnetic and dielectric properties of $Mn_2V_2O_7$. *Solid State Commun.* **2016**, *228*, 10−15.

(12) Sannigrahi, J.; Adroja, D. T.; Perry, R.; Gutmann, M. J.; Petricek, V.; Khalyavin, D. Commensurate to incommensurate magnetic phase transition in honeycomb-lattice pyrovanadate $Mn_2V_2O_7$. *Phys. Rev. Mater.* **2019**, *3*, 113401−113408.

(13) He, Z.; Ueda, Y.; Itoh, M. Martensitic-like transition in $Mn_2V_2O_7$ single crystals. *Solid State Commun.* **2008**, *147*, 138−140.

(14) Sun, Y. C.; Ouyang, Z. W.; Xiao, Y.; Su, Y.; Feng, E.; Fu, Z.; Jin, W. T.; Zbiri, M.; Xia, Z. C.; Wang, J. F.; Rao, G. H. Honeycomb-lattice antiferromagnet $Mn_2V_2O_7$: A temperature dependent X-ray diffraction, neutron diffraction and ESR study. *Mater. Res. Express* **2017**, *4*, 46101−46111.

(15) Wu, H. C.; Hsieh, D. J.; Yen, T. W.; Sun, P. J.; Kakarla, D. C.; Her, J. L.; Matsuda, Y. H.; Chang, C. K.; Lai, Y. C.; Gooch, M.; Deng, L. Z.; Webber, K. G.; Lee, C. A.; Chou, M. M. C.; Chu, C. W.; Yang, H. D. Pressure and magnetic field effects on ferroelastic and antiferromagnetic orderings in honeycomb-lattice $Mn_2V_2O_7$. *Phys. Rev. B* **2020**, *102*, 75130−75137.

(16) Sambandam, B.; Soundharrajan, V.; Song, J.; Kim, S.; Jo, J.; Duong, P. T.; Kim, S.; Mathew, V.; Kim, J. Investigation of Li-ion storage properties of earth abundant β-$Mn_2V_2O_7$ prepared using facile green strategy. *J. Power Sources* **2017**, *350*, 80−86.

(17) Xia, D.; Xu, S.; Wang, W.; Wang, D.; Wu, M.; Gong, F. Pure-phase β-$Mn_2V_2O_7$ interconnected nanospheres as a high-performance lithium ion battery anode. *Chem. Commun.* **2020**, *56*, 8043−8046.

(18) Xia, D.; Gao, H.; Li, M.; Gong, F.; Li, M. Transition metal vanadate electrodes in lithium-ion batteries: A holistic review. *Energy Storage Mater.* **2021**, *35*, 169−191.

(19) Ravindra, P.; Athresh, E.; Ranjan, R.; Raghavan, S.; Avasthi, S. Effect of annealing on performance of solar cells with new oxide absorber $Mn_2V_2O_7$. *IEEE 44th Photovoltaic Specialist Conference (PVSC)*, 2017; pp 2395−2399.

(20) Zhao, L.; Lin, S.; Bi, K.; Liang, C.; Du, Y.; Liu, J.; Yang, H.; Fan, D.; Wang, Y.; Lei, M. Manganese vanadium oxide hollow microspheres: A novel electrocatalyst for oxygen reduction reaction. *J. Solid State Electrochem.* **2017**, *21*, 1743−1749.

(21) Xin, Y.; Li, H.; Zhang, N.; Li, Q.; Zhang, Z.; Cao, X.; Hu, P.; Zheng, L.; Anderson, J. A. Molecular-level insight into selective catalytic reduction of NO_x with NH_3 to N_2 over a highly efficient bifunctional V_α-MnO_x catalyst at low temperature. *ACS Catal.* **2018**, *8*, 4937−4949.

(22) Xing, X.; Liu, R.; Cao, K.; Kaiser, U.; Zhang, G.; Streb, C. Manganese vanadium oxide-N-doped reduced graphene oxide composites as oxygen reduction and oxygen evolution electrocatalysts. *ACS Appl. Mater. Interfaces* **2018**, *10*, 44511−44517.

(23) Toma, F. M.; Cooper, J. K.; Kunzelmann, V.; McDowell, M. T.; Yu, J.; Larson, D. M.; Borys, N. J.; Abelyan, C.; Beeman, J. W.; Yu, K. M.; Yang, J.; Chen, L.; Shaner, M. R.; Spurgeon, J.; Houle, F. A.; Persson, K. A.; Sharp, I. D. Mechanistic insights into chemical and photochemical transformations of bismuth vanadate photoanodes. *Nat. Commun.* **2016**, *7*, 12012−12023.

(24) Zhou, L.; Yan, Q.; Yu, J.; Jones, R. J. R.; Becerra-Stasiewicz, N.; Suram, S. K.; Shinde, A.; Guevarra, D.; Neaton, J. B.; Persson, K. A.; Gregoire, J. M. Stability and self-passivation of copper vanadate photoanodes under chemical, electrochemical, and photoelectrochemical operation. *Phys. Chem. Chem. Phys.* **2016**, *18*, 9349−9352.

(25) Knöppel, J.; Kormányos, A.; Mayerhöfer, B.; Hofer, A.; Bierling, M.; Bachmann, J.; Thiele, S.; Cherevko, S. Photocorrosion of WO_3 photoanodes in different electrolytes. *ACS Phys. Chem. Au* **2021**, DOI: 10.1021/acsphyschemau.1c00004.

(26) Nair, V.; Perkins, C. L.; Lin, Q.; Law, M. Textured nanoporous Mo:$BiVO_4$ photoanodes with high charge transport and charge transfer quantum efficiencies for oxygen evolution. *Energy Environ. Sci.* **2016**, *9*, 1412−1429.

(27) Ilton, E. S.; Post, J. E.; Heaney, P. J.; Ling, F. T.; Kerisit, S. N. XPS Determination of Mn oxidation states in Mn (hydr)oxides. *Appl. Surf. Sci.* **2016**, *366*, 475−485.

(28) Biesinger, M. C.; Payne, B. P.; Grosvenor, A. P.; Lau, L. W. M.; Gerson, A. R.; Smart, R. S. C. Resolving surface chemical states in XPS analysis of first row transition metals, oxides and hydroxides: Cr, Mn, Fe, Co and Ni. *Appl. Surf. Sci.* **2011**, *257*, 2717−2730.

(29) Nesbitt, H. W.; Banerjee, D. Interpretation of XPS Mn(2p) Spectra of Mn oxyhydroxides and constraints on the mechanism of MnO_2 precipitation. *Am. Mineral.* **1998**, *83*, 305−315.

(30) Mesmer, R. E.; Baes, C. F.; Sweeton, F. H. Acidity measurements at elevated temperatures. VI. Boric acid equilibria. *Inorg. Chem.* **1972**, *11*, 537−543.

(31) Jin, J.; Walczak, K.; Singh, M. R.; Karp, C.; Lewis, N. S.; Xiang, C. An experimental and modeling/simulation-based evaluation of the efficiency and operational performance characteristics of an integrated, membrane-free, neutral pH solar-driven water-splitting system. *Energy Environ. Sci.* **2014**, *7*, 3371−3380.

(32) Ravensbergen, J.; Abdi, F. F.; van Santen, J. H.; Frese, R. N.; Dam, B.; van de Krol, R.; Kennis, J. T. M. Unraveling the carrier dynamics of $BiVO_4$: A femtosecond to microsecond transient absorption study. *J. Phys. Chem. C* **2014**, *118*, 27793−27800.

(33) Cooper, J. K.; Reyes-Lillo, S. E.; Hess, L. H.; Jiang, C.-M.; Neaton, J. B.; Sharp, I. D. Physical origins of the transient absorption spectra and dynamics in thin-film semiconductors: The case of $BiVO_4$. *J. Phys. Chem. C* **2018**, *122*, 20642−20652.

(34) Liu, J.; Leng, J.; Wang, S.; Zhang, J.; Jin, S. Artifacts in transient absorption measurements of perovskite films induced by transient reflection from morphological microstructures. *J. Phys. Chem. Lett.* **2019**, *10*, 97−101.

(35) Suzuki, Y.; Murthy, D. H. K.; Matsuzaki, H.; Furube, A.; Wang, Q.; Hisatomi, T.; Domen, K.; Seki, K. Rational interpretation of correlated kinetics of mobile and trapped charge carriers: Analysis of ultrafast carrier dynamics in $BiVO_4$. *J. Phys. Chem. C* **2017**, *121*, 19044−19052.

(36) Selim, S.; Pastor, E.; García-Tecedor, M.; Morris, M. R.; Francàs, L.; Sachs, M.; Moss, B.; Corby, S.; Mesa, C. A.; Gimenez, S.; Kafizas, A.; Bakulin, A. A.; Durrant, J. R. Impact of oxygen vacancy occupancy on charge carrier dynamics in $BiVO_4$ photoanodes. *J. Am. Chem. Soc.* **2019**, *141*, 18791−18798.